Nuclear Instruments and Methods in Physics Research A 1073 (2025) 170284

Contents lists available at ScienceDirect

Nuclear Inst. and Methods in Physics Research, A

journal homepage: www.elsevier.com/locate/nima

Exploring spatial resolution enhancements on IMAT for steel corrosion studies

Vicky Ullas Mirashi [a,b,c], Winfried Kockelmann [c], Nikil Kapur [b], Anna Fedrigo [c], Manuel Morgano [d,e], Thawatchart Chulapakorn [e], Adrian Losko [f], Alexander Wolfertz [f], Anton S. Tremsin [g], Adriana Matamoros-Veloza [a,h,*]

[a] Faculty of Engineering and Physical Sciences, University of Leeds, Leeds, LS2 9JT, UK
[b] School of Mechanical Engineering, University of Leeds, Leeds, LS2 9JT, UK
[c] STFC-Rutherford Appleton Laboratory, ISIS Facility, Harwell, OX11 0QX, UK
[d] Paul Scherrer Institut, Forschungsstrasse 111, Villigen, 5232, Switzerland
[e] European Spallation Source, Partikelgatan 2, Lund, 224 84, Sweden
[f] Heinz Maier-Leibnitz Zentrum (MLZ), Technische Universität München, Garching, Germany
[g] University of California at Berkeley, Space Sciences Laboratory, Berkeley, CA, 94720, USA
[h] School of Chemistry, University of Leeds, Leeds, LS2 9JT, UK

ARTICLE INFO

Keywords:
Neutron imaging
Corrosion
Spatial resolution
IMAT
Fiber optics taper
Timepix

ABSTRACT

Neutron imaging offers benefits over X-rays for steel corrosion studies including deep penetration and high sensitivity to some light elements such as hydrogen. However, the resolution is frequently at or below the thickness of the corroded layer. This work demonstrates two approaches to enhance the spatial resolution on IMAT at the ISIS neutron source. The first approach shows that a fiber optics taper attached to an optical camera box for white beam imaging can achieve a spatial resolution down to 15 μm. The second approach uses event centroiding with a Timepix3-based detector for diffraction contrast imaging achieving a spatial resolution of 30 μm. These results support advances in corrosion and degradation studies of steel using neutron imaging.

1. Introduction

The unique ability of neutrons to penetrate deep into materials makes the conduction of non-destructive scientific research possible, allowing the performance of residual strain analysis [1,2] and quantification of internal cracks, which are examples of key characterization parameters in the study of materials [3]. Neutrons offer benefits different from X-rays or electrons such as sensitivity to light elements (e.g., hydrogen and lithium) and a high penetrating capability. Neutron imaging has shown to be the most effective way for examining thick and large metal samples (e.g., iron, nickel, zirconium, and tungsten) that are otherwise difficult to image using other methods. This technique allows the conduction of attenuation-based studies to differentiate between isotopes, and to achieve magnetic imaging of internal magnetic fields [4]. Although neutron imaging offers benefits over other analysis techniques (e.g., imaging using electrons and X-rays), achieving high spatial resolution remains a challenge [4]. Spatial resolution is influenced by several parameters including neutron flux, neutron energy, sample-to-detector distance, size of sample, camera resolution, data binning, data processing filter and beam divergence determined by the collimation ratio [5,6]. Furthermore, spatial resolution is a crucial parameter to quantify 2D and 3D imaging data from thin films or coated materials (e.g., surface corrosion layers), thus the need to improve imaging resolution remains.

Spatial resolution is the ability of the instrument to resolve two neighboring points. It is commonly expressed in terms of line pairs per millimeter (Lp/mm) where line pairs are a sequence of bright and dark lines [7]. The higher the spatial resolution, the more information can be obtained from the underlying structure of a sample. The rising demand for high resolution applications makes neutron facilities constantly strive towards better resolution. Most neutron instruments have limited spatial resolution in the tens of microns; however, some high-flux neutron facilities currently achieve better than 10 μm [8]. Resolution improvements have been demonstrated on neutron imaging stations with thermal (NEUTRA) and cold (ICON) neutrons at the Swiss neutron spallation source (SINQ) of the Paul Scherrer Institut (PSI, Switzerland)

* Corresponding author. Faculty of Engineering and Physical Sciences, University of Leeds, Leeds, LS2 9JT, UK.
E-mail address: A.MatamorosVeloza@leeds.ac.uk (A. Matamoros-Veloza).

https://doi.org/10.1016/j.nima.2025.170284
Received 12 November 2024; Received in revised form 20 January 2025; Accepted 30 January 2025
Available online 6 February 2025

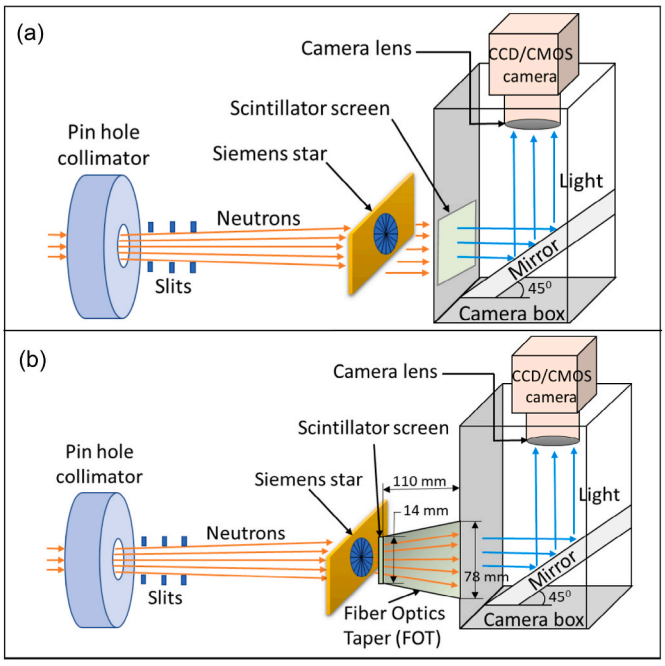

Fig. 1. (a), (b) Schematic setup of the IMAT beamline showing CCD and CCD + taper arrangement.

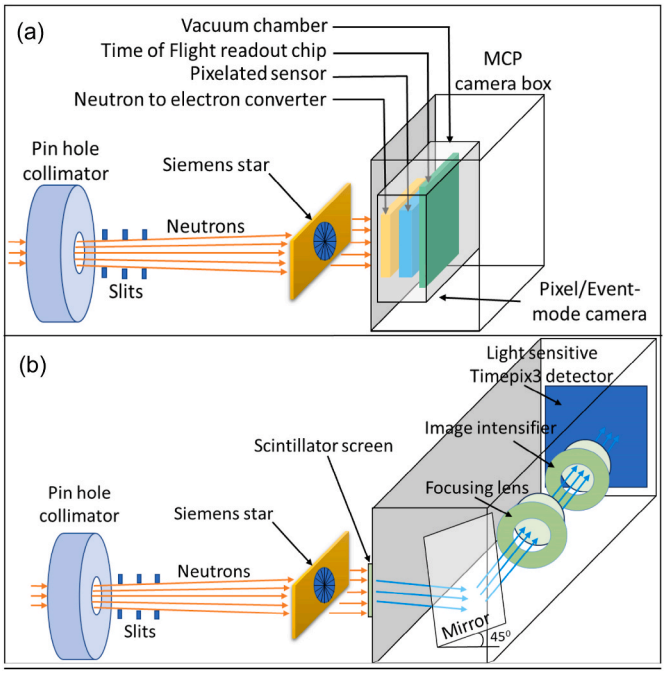

Fig. 2. (a), (b) Schematic setup of the IMAT beamline showing the MCP and LumaCam arrangement.

using a Fiber Optics Taper (FOT) to achieve a resolution of 15 μm [9]. A FOT is a device that can magnify an optical image from one end of the device to the other end with a larger size. Furthermore, resolution enhancements to 7.6 μm [10] were achieved with a 'neutron microscope' at PSI, using a neutron sensitive ^{157}Gd enriched gadolinium oxysulfide (Gadox) scintillator for high detection efficiency and a 5:1 lens for optimized light collection and magnification. The Neutron and X-ray Tomograph (NeXT) beamline at Grenoble, having the world's highest flux on a neutron imaging station, allows for a high degree of collimation with short exposure time along with complementary X-ray imaging. A gadolinium gallium garnet $Gd_3Ga_5O_{12}$:Eu (GGG:Eu) single crystal scintillator was used to achieve resolution below 4 μm [11,12]. The National Institute for Standards and Technology (NIST, USA) have used image intensifiers and Gadox scintillators as well as microchannel plates (MCP) with cross wire readout [13] to achieve enhanced resolutions of ~20 μm and 13 μm, respectively. Other techniques available to enhance resolution for white beam applications include scintillators such as gadolinium oxysulfide and gadolinium aluminium gallium garnet [14,15], and Li-based detectors [16,17]. A microchannel plate (MCP) detector was used in conjunction with a centroiding technique [18,19] to achieve a resolution below 20 μm. This has also been demonstrated on IMAT [20]; however, the setup required long acquisition times of several hours to collect a single radiogram. Most neutron imaging facilities employ standard optical systems to capture the photons coming from a scintillator screen, and many of the above-mentioned approaches cannot be applied on IMAT as some of them involve significant modifications to the setups, namely through increase of neutron source flux and improvement of neutron transport from source to beamline [21–23].

Spatial resolution for wavelength-resolved imaging and Bragg edge analysis is generally much lower for the same measurement time compared to white beam imaging. This is due to limitations in neutron flux and long scan-times, as neutrons are distributed over a multitude of wavelength channels, for example, when filling time channels in a time-of-flight (TOF) setup or for a wavelength scan of a monochromatized neutron beam. Typically, spatial resolution on TOF instruments is around 200 μm or more, when using an MCP with Timepix readout with 55 μm pixels [24,25]. A LumaCam detector, a Timepix-3 based system with the same pixel size and high detection efficiency is capable of extending resolution to sub-pixel values using event centroiding [26].

Neutron imaging is often required for materials studies, and diffraction techniques are typically needed for characterization. Limited neutron flux restricts the reach to higher resolution, while high flux allows for smaller pinhole diameter and high L/D (i.e., L:Pin hole to sample distance, D:Aperture diameter of collimator) as well as sufficient counting statistics in order to enhance resolution. Hence, resolution improvements are explored in this work for both conventional neutron imaging and Bragg edge diffraction imaging. Surface imaging is crucial to elucidate metal degradation in combination with chemical and electrochemical characterization. A field urgently requiring advances in imaging techniques is corrosion science. Steel corrosion has been responsible for global infrastructure failures with detrimental human and environmental effects. Two main types of corrosion affect carbon steel materials in CO_2 environments (e.g., oil and gas, CO_2 transport), general and localized corrosion. Siderite ($FeCO_3$) is the main product of general corrosion, formed from the dissolution of iron from steel, but the most harmful type of corrosion is localized corrosion or pitting, due to its stochastic nature and poorly understood process [27]. Corrosion layers range from microns up to tens of microns depending on environment conditions, whereas localized pits can be considerably larger, reaching hundreds of microns [28]. Visualizing gradual degradation of steel, growth of corrosion films and corrosion pits in 3D requires improvement of spatial resolution on IMAT.

Spatial resolution on the medium flux Imaging and Materials Science (IMAT) instrument [29] is 60 μm for white beam imaging and typically more than 100 μm for Bragg edge imaging. Hence, resolution enhancements were explored to improve imaging capabilities and to support corrosion studies well below 60 μm. A Fiber Optics Taper (FOT) coupled to existing camera boxes was investigated to achieve higher resolution for white beam neutron imaging, working on the principle of optical magnification without requiring significant changes to the detection system [9]. The magnification approach helped to scale down the effective pixel size improving spatial resolution, however at the expense of field of view. The resolution was evaluated in 2D and 3D by applying the Modulation Transfer Function (MTF) approach [30]. For energy resolved imaging, two different time of flight imaging detection systems based on Timepix readout were used to study resolution. In each

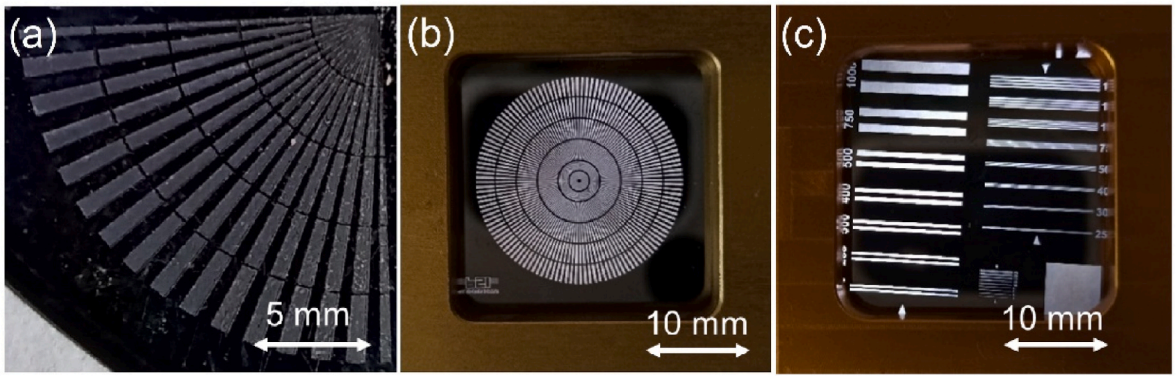

Fig. 3. (a) Triangular Siemens star (b) circular Siemens star (c) linear mask used to evaluate 2D spatial resolution for CCD, CCD + taper and Timepix systems. All photographs were captured using an optical camera.

Table 1
Experimental parameters used for conducting studies at IMAT. NR: Neutron radiography, NT: Neutron tomography, BEI: Bragg edge imaging, CCD: Charge coupled device, CMOS: Complementary Metal Oxide Semiconductor, MCP: Multi-channel plate, FOT: Fiber optics taper, TOF: Time of Flight, l: Sample-Scintillator gap, L: Beam length (10.2 m), D: Pin hole diameter. Tomography step angle for $NT_1 = 0.718°$ and $NT_2 = 0.576°$, respectively.

Sample details	Camera, setup	Pixel size (μm)	Scintillator type, thickness (μm)	D (mm), L/D	Geometric blur, l/(L/D), (μm)	Exp. time per scan (s)
Triangular (16 × 16 mm) and circular mask (25 × 25 mm)	CCD, NR	30	LiF + ZnS, 60	80, 127.5	19.6	60
Triangular (16 × 16 mm) and circular mask (25 × 25 mm)	CCD, FOT, NR	9	Gadox + LiF, 30	60, 170	14.7	600
Circular mask (25 × 25 mm)	CMOS, FOT, NR	6	^{157}Gadox, 4	40, 255	9.8	30
Linear and circular mask (25 × 25 mm)	MCP, BEI	55	TOF timepix	40, 255	72.5	900
Linear and circular mask (25 × 25 mm)	LumaCam, BEI	15	Gadox, 20	60, 170	14.7	600
Steel spheres (Ø2mm)	CCD, NT_1	30	LiF + ZnS, 60	60, 170	20.6	80
Steel (Ø2mm) and zirconia spheres (Ø0.5 mm)	FOT, NT_2	9	Gadox + LiF, 30	80, 127.5	27.4	180
X65 steel sample with siderite film (Ø12mm)	MCP, BEI	55	TOF timepix	80, 127.5	188.2	10hrs
X65 steel sample with siderite film (Ø12mm)	LumaCam, BEI	15	Gadox, 20	60, 170	41.2	2hrs

case, resolving power was tested with resolution masks, steel spheres and a corroded steel sample.

2. Experimental arrangement

2.1. Beamline setup

The experiments were carried out at the Imaging and Material science (IMAT) cold neutron beamline on target station 2 of the ISIS Facility, UK [29]. IMAT provides imaging characterization techniques such as neutron radiography, neutron tomography, and Bragg edge diffraction contrast imaging [31]. Ten pulses of neutrons per second are produced in the spallation source tungsten target. Neutrons are slowed-down to cold neutrons with the help of a liquid hydrogen moderator, maintained at 18 K, providing neutron wavelengths ranging between 0.5 and 10 Å with a maximum flux at about 2.6 Å. Two 10 Hz double disk choppers enable selection of a neutron energy band, typically between 1 and 7 Å (81.8 meV–1.6 meV). A 10-Hz "T0" chopper filters out fast neutrons and gamma radiation at the start of a pulse. A pinhole collimator made of 10 mm thick B_4C is employed in the path, at 46 m from the source, to control the beam divergence. A selector wheel has six collimators at 10 m from the sample position with L/D ratios between 100 and 500 [29].

Figs. 1 and 2 illustrate a schematic representation of all setups with Siemens star resolution masks on IMAT. Once the neutrons strike the sample (at a distance of L∼10 m from the pinhole collimator), a fraction of those neutrons pass through the sample and a portion of them are absorbed by a scintillator screen and converted into photons (for Charge-Coupled Device (CCD) [32,33], Complementary Metal Oxide Semiconductor (CMOS) [34] and LumaCam [26] setup) or converted by a neutron sensitive microchannel plate sensor to electrons (for MCP [24] setup). The camera box was positioned on the instrument with the help of a robotic arm. The light-tight camera box contains the neutron converter (scintillator) plate, a mirror at a 45° angle relative to the beam direction, a focusing lens and a CCD or CMOS camera module (Fig. 1). The sample was placed on a 360° rotating stage along with linear translations in x, y, z axes to allow adjustment of the sample in relation to the detector [29]. To minimize geometric blur, the sample of interest needs to be placed close to the detector (∼1 mm gap). The geometric blur is given by l*(D/L), where l = distance from center of sample to scintillator, D = diameter of pinhole collimator, L = distance from collimator to sample center [35].

The CCD camera setup (Fig. 1a) consisted of a scintillator of 60 μm thickness (NR-Al-1-60, 90 × 90 mm^2 ZnS/^{6}LiF, 2:1 [36]) and an ANDOR IKON-L CCD camera with 2048 × 2048 pixels, 135 mm focusing lens, F-stop value of 2.0, providing a pixel size of 31.4 μm for a field of view of about 65 × 65 mm^2. The setup with a Fiber Optics Taper (FOT, Incom Inc, USA) (Fig. 1b) consisted of a series of hexagonal shaped Boron glass fibers resembling a honeycomb structure with a magnification ratio of 6:1 [37]. These glass filaments direct the photons to propagate in a single direction, while each fiber guides photons to prevent crosstalk. The taper dimensions were 110 mm in length, 14 mm in diameter on one side and 78.25 mm in diameter on the opposite side. The effective field of view for this taper was about 6 mm in diameter. A scintillator of 30 μm thickness (NR-Al-20-30, 30 × 30 mm^2, Gd_2O_2S:Tb/^{6}LiF (20%) [36]) was attached to the smaller side of the taper. The above-mentioned ANDOR IKON-L CCD camera was used with a 105 mm focusing lens, F-stop 2.0 and with 9 μm effective pixel size. Additional measurements

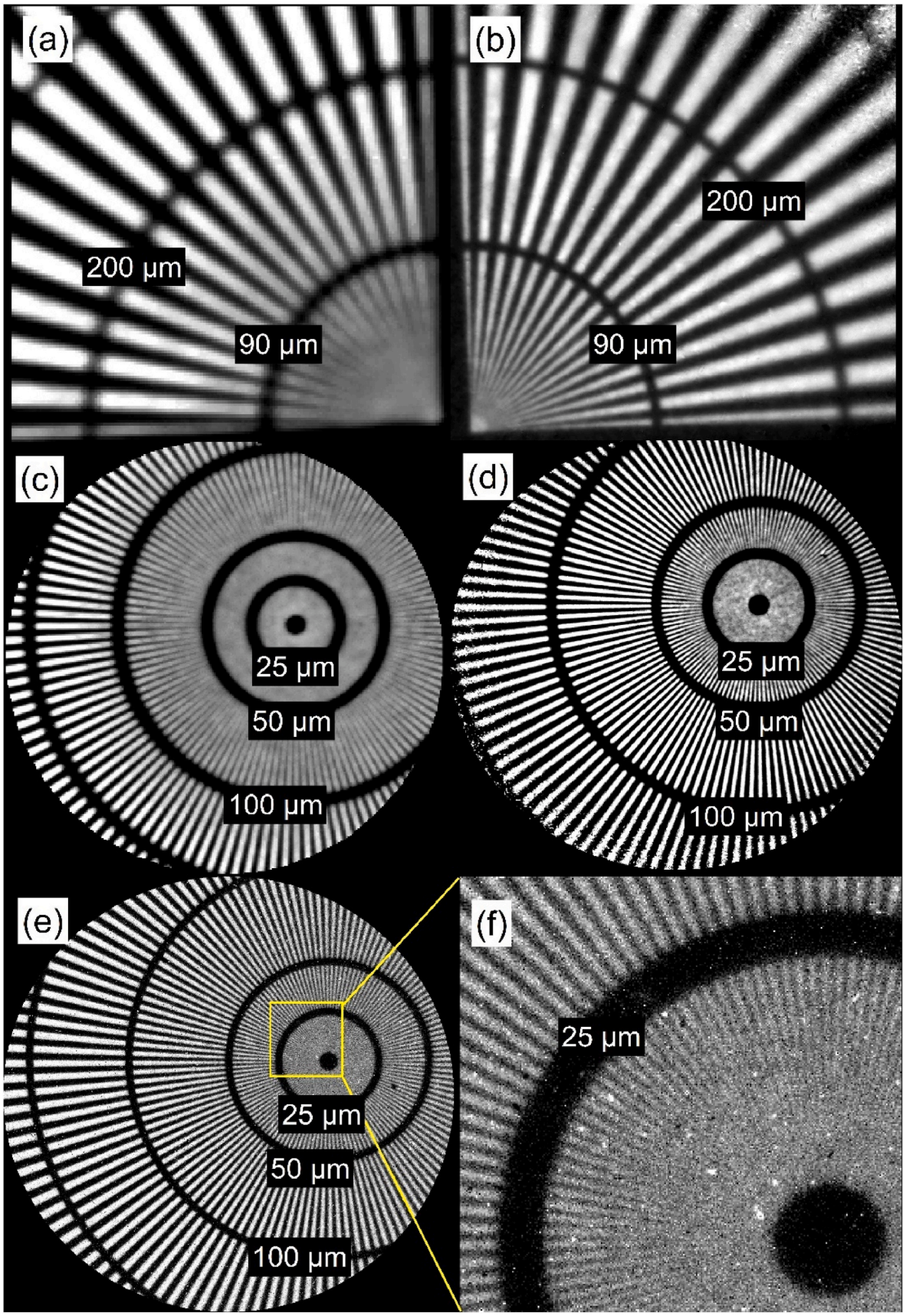

Fig. 4. (a), (c) Triangular and circular Siemens star mask radiograms for CCD setup with 60 µm scintillator (b), (d) Triangular and circular Siemens star mask images for CCD + taper setup with 30 µm scintillator, (e) Circular Siemens star mask for CCD + taper setup with 4 µm scintillator (f) Enlarged view of the chosen region highlighted in (e).

Table 2
Tabulated values of line pairs per mm and resolution for white beam imaging (from Fig. 5).

Setup	Siemens star type	Scintillator thickness (μm)	Line pairs per mm (mm^{-1})	Resolution (μm)
CCD	triangular	60	8.56	58.4
CCD	circular	60	8.71	57.4
CCD + taper	triangular	30	16.84	29.7
CCD + taper	circular	30	17.67	28.3
CMOS + taper	circular	4	38.87	12.9

were performed with a FOT attached to an ANDOR Zyla 4.2 PLUS CMOS camera box, similar to the CCD arrangement (Fig. 1b). The small end of the taper featured a thin scintillator of 4 μm thickness (made of isotopic ^{157}Gd-enriched Gadox [38]). The setup employed a 135 mm lens resulting in a field of view of 12 × 12 mm^2 and effective pixel size of 6.31 μm.

The two detectors used for energy resolved imaging, microchannel plate (MCP) and LumaCam, are illustrated in Fig. 2a and b. The MCP detector operates on the principle of converting neutrons to electrons (in a boron ^{10}B and gadolinium (Gd) doped neutron-sensitive MCP). This is followed by amplification in front of 2 × 2 tiled Timepix readout chips with 2800 time channels (with a timebin width of 20 μs from 10 to 48 ms and 40 μs from 48 to 95 ms). With 512 × 512 pixels, each having a pixel size of 55 μm, the field of view is 28 × 28 mm^2 [24,39,40]. The MCP sensor was located at a distance of 17 mm from the front face of the detector housing. The LumaCam [26] TOF system functions by converting neutrons to photons using a 20 μm Gadox scintillator sheet, 45-degree mirror, light focusing system, P47 phosphor image intensifier, and a light sensitive Timepix3 detector (Amsterdam Scientific) with 55 μm pixel size. This microscopy arrangement is similar to the neutron microscope concept at PSI [10]. By means of event collection and processing, image stacks were saved with a pixel size of 15 μm using 4000 active time channels for each pixel having a 25 μs channel width. The field of view was 7 × 7 mm^2 and the neutron flight path from source to detector was 56.5 m for both detectors. It can be noted that while both pixel detectors operate with 55 μm pixel readout sensors, the centroiding mode of the LumaCam provides time-of-flight spectra for 15 μm subpixels. Therefore, LumaCam achieves higher spatial resolution for Bragg edge imaging compared to the MCP, however with a 16 times smaller field of view.

2.2. Details of samples

2D resolution was evaluated using three different resolution masks, while 3D resolution was examined using steel spheres. 2D resolution was evaluated by using triangular and circular 'Siemens stars' and a linear mask of known standard dimensions (Fig. 3). The triangular mask consists of a silicon substrate with 7 μm thick gadolinium material deposited on the surface. The circular and linear masks consist of quartz wafer substrates with 5 μm gadolinium deposition, mounted onto an aluminum frame (Fig. 3) with resolution values printed in μm on the linear mask. 3D resolution was evaluated according to Kaestner [41] using 2 mm steel and 0.5 mm zirconia spheres, with the small ones filling the spaces between the bigger spheres, placed inside a thin-walled cylindrical aluminum holder of 3 mm diameter. For the energy-resolving detectors, resolution masks were used as well as a corroded API 5L X65 grade low carbon steel [42] sample of 12 mm diameter with a ~40 μm thick siderite corrosion layer on the top surface.

2.3. Methodology

Radiography and tomography data were collected with experimental parameters as shown in Table 1. Processing these data involved first outlier removal and then flat fielding using open beam and dark field images. For each white-beam dataset, 5–20 radiograms were collected. They were averaged and scaled to account for beam fluctuations, whereas for energy resolved imaging the summed image was used to normalize open beam images. For tomography, in addition to these steps, the removal of data stripe artifact and region of interest normalization were performed before reconstruction. This process was performed using the iterative PDHG-TV (Primal-dual hybrid gradient with total variation regularisation) algorithm within the Core Imaging Library (CIL), with 200 iterations as implemented in the Mantid Imaging tool [43]. The reconstructed data were visualized in 3D using Avizo [44], and a segmentation method (watershed algorithm) was employed to differentiate between steel and zirconia spheres.

To determine the imaging resolution, we used the Modulation Transfer Function (MTF) method for both 2D and 3D imaging [45,46]. The first step for this method was to select an edge of the Siemens star masks for 2D and a reconstructed slice of the sphere (50% of the sphere height) for 3D. A perpendicular line was drawn across the edge of the mask-spoke or the slice edge. An ImageJ software plugin was used to directly derive the MTF plot [47,48]. For MTF calculations, a minimum cutoff of 10% was taken to quantify the spatial resolution for 10% contrast difference between features. The MTF curve intersecting the

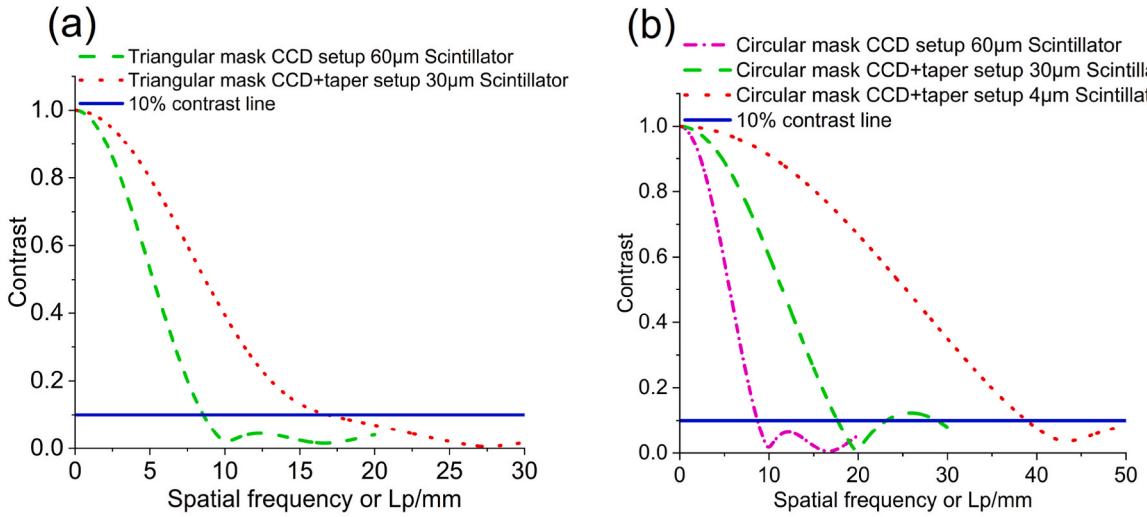

Fig. 5. (a) Triangular mask MTF curves for CCD and CCD + taper setups, (b) Circular mask MTF curves for CCD and CCD + taper setups.

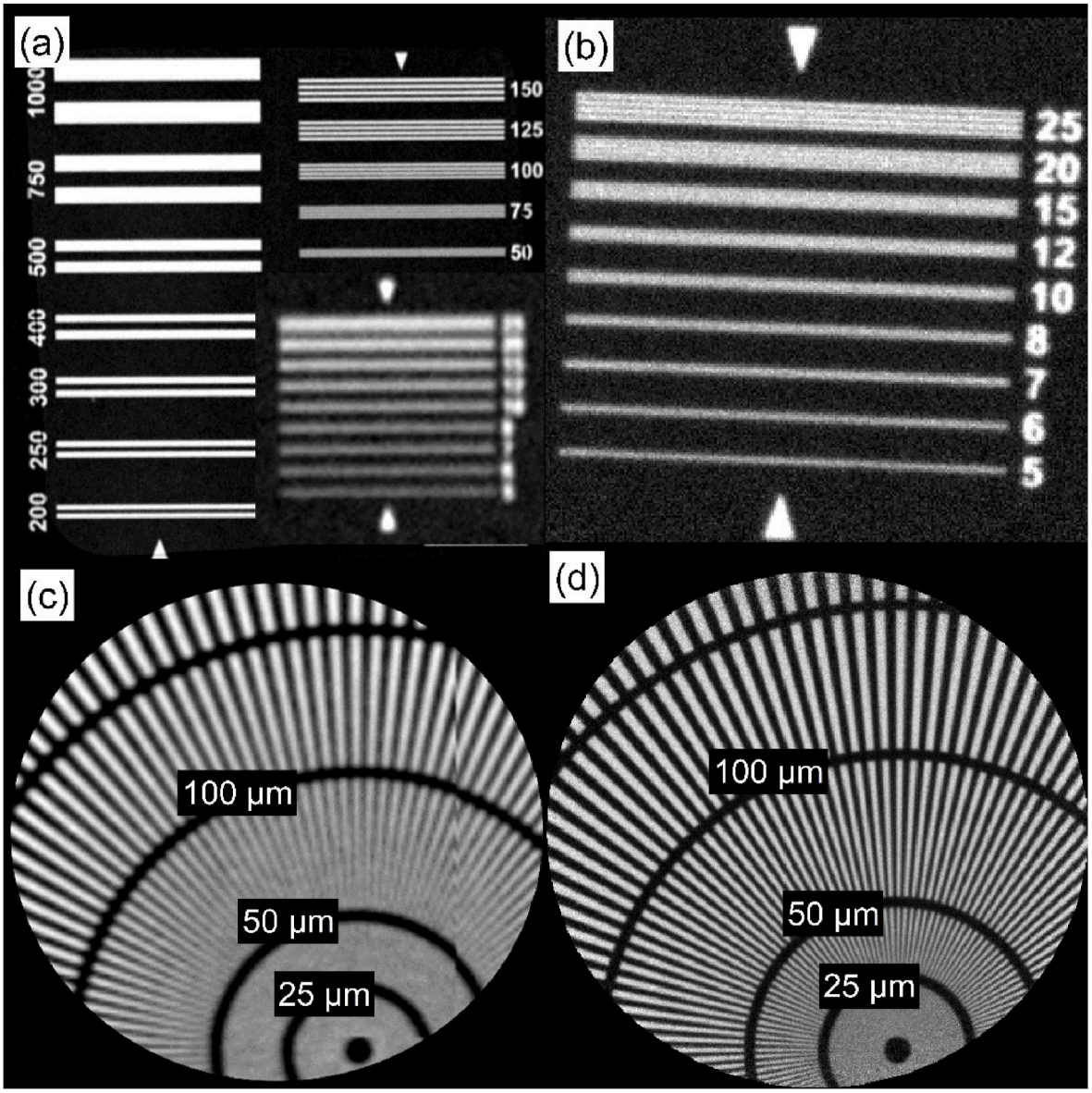

Fig. 6. (a), (c) Linear and circular Siemens star mask for MCP setup, (b), (d) linear and circular Siemens star mask for LumaCam setup. Summation of neutron wavelengths from 1 to 7 Å was used to obtain the radiographs.

10% contrast line yielded the corresponding spatial frequency or Lp/mm on the x-axis. By taking the inverse of this value, and division by two, the spatial resolution of the setup was obtained [49,50].

As an example of a practical application, a corroded X65 steel sample with a siderite film on the surface was scanned at IMAT using the experimental parameters listed in Table 1. The sample was corroded prior to imaging in a glass reactor containing 1-liter brine (3.5% NaCl) solution and a constant supply of CO_2 gas (0.2 LPM air) provided throughout. The corrosion treatment was performed at 60 °C for a period of 72 h maintained a constant pH of 6.8 and a voltage supply of ± 15 mV. For the MCP setup, data were collected for a total of 10 h, split into 4, 4 and 2 h, and overlap corrected [51]. For the LumaCam setup, the collection time was 2 h. For both detectors and for the resolution mask images, data were first summed along the TOF axis (individually for sample and open-beam images) and then flat fielded. For Bragg edge analysis, however, intensity-versus-TOF curves were extracted and converted to intensity-versus-wavelength curves using ImageJ and Mantid Imaging for selected regions of interest (ROIs). Sample data were divided by the corresponding open-beam data in order to visualise the Bragg edge curves as transmission profile plots. Four ROIs were selected: two in the steel region and two in the siderite region. The Bragg curves were smoothened using a Savitzky-Golay filter with a window size of 30 using the Origin software [52].

3. Results and discussions

3.1. 2D resolution evaluation for white beam imaging setup

Triangular and circular masks were used to test the CCD/CMOS setup with and without external FOT attachment (Fig. 4). As the taper setup had a smaller pixel size and used a thinner scintillator, exposure times were increased (Table 1) to counter decreasing statistics. Considering the circular mask, the line pairs per millimeter for 10% contrast were found to be 8.71 mm^{-1} (Table 2), and the corresponding spatial resolution was 57.4 µm for the CCD setup and 28.3 µm for the taper setup. The MTF plots for the masks along with the radiograms are shown in Fig. 5. It is evident that the spatial resolution has improved from 60 µm to 30 µm with the installation of the taper. The Siemens star mask images

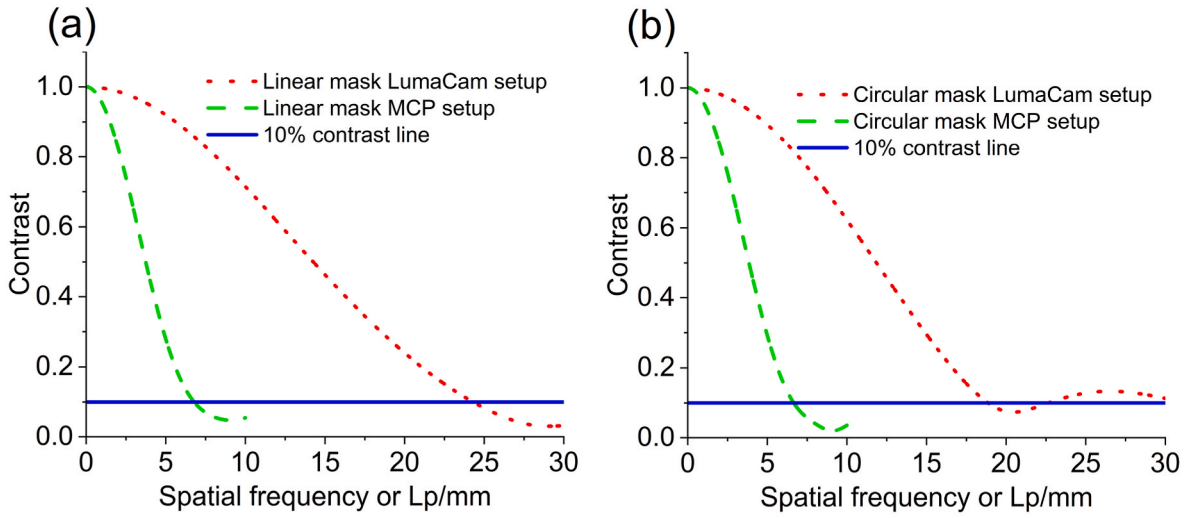

Fig. 7. (a) Triangular mask MTF curves for MCP and LumaCam setups, (b) Circular mask MTF curves for MCP and LumaCam setups. Images for neutron wavelengths from 1 to 7 Å were summed prior to the MTF analysis.

Table 3
Tabulated values of line pairs per mm, resolution for energy resolved imaging (from Fig. 7).

Setup	Siemens star type	Line pairs per mm (mm^{-1})	Resolution (μm)
MCP	linear	6.09	82.1
MCP	circular	6.48	77.2
LumaCam	linear	18.27	27.4
LumaCam	circular	18.87	26.5

provide a visual representation of the resolution enhancement.

In addition to the 30 μm scintillator, the FOT setup was also tested with a thin isotopic Gadox scintillator of 4 μm thickness. The ^{157}Gadolinium-enriched Gadox scintillator used in the experiment has higher efficiency of neutron absorption and the resolution achieved was ~13 μm (Table 2), surpassing all the previous high-resolution setups at IMAT. The grey values in this test were very low (about 400, which is close to dark counts of about 300), due to the use of thinner scintillator and the image acquisition time of 30 s. While it is beneficial to attempt higher resolution with a thinner scintillator, it is at the cost of the longer measuring times for adequate levels of grey values.

3.2. 2D resolution evaluation for energy resolved imaging setup

The evaluation of resolution for energy resolved imaging (MCP and LumaCam) was performed with the linear and circular masks (Fig. 6). The small pixel size and thin scintillator for the latter was compensated by using larger pinhole diameter (60 mm) (Table 1). Data were collected as image stacks at discrete wavelengths. For resolution determination, the MTF curve was plotted correspondingly (Fig. 7). The spatial resolutions for MCP and LumaCam setups were 80 μm and 30 μm respectively (Table 3). The LumaCam resolution allowed obtaining Bragg edges for thin corrosion films (see section 3.4). Additionally, the effect of the neutron wavelength on resolution was not significant for either setup (Fig. S1 and Table S1). A vertical line artifact on the right-hand side of the MCP image of the circular Siemens star in Fig. 6c is due to a split of the sensor area between two Timepix quadrants of the MCP detector.

3.3. 3D resolution evaluation using steel spheres for white beam imaging

Evaluation of 3D resolution is essential to study material degradation with features typically in the range of μm to tens of μm (e.g., steel corrosion). Steel spheres were used for this evaluation, as zirconia spheres have poorer visibility and suffer from lower signal-to-background due to the high neutron transmission (Fig. 8). Reconstructed slices for both CCD and the taper setups were analyzed using the MTF method (Fig. 9), similar to the 2D resolution calculations described in section 3.1. The resolution of the reconstructed slices was assumed to represent the entire sample in 3D space. Using the taper setup, the resolution dropped slightly relative to the 2D resolution measurement from 28.3 μm to 32.5 μm due to small increase in geometric blur (Tables 2 and 4). This difference is within the MTF analysis error and not considered significant. Nevertheless, a larger sample may result in a higher geometric blur and a more noticeable difference in spatial resolution. It is evident that the taper attachment improved the 3D resolution on IMAT by nearly a factor of two. This resolution enhancement of IMAT will aid studies of CO_2 induced corrosion on steel, despite refraction edge effects at the air-steel interface, as dimensions of features now fall within the instrument's range. For the CCD setup, the 3D spatial resolution was 56.3 μm (Table 4), nearly the same value obtained for 2D resolution (Table 2), indicating that a slight increase of sample-center to scintillator distance and geometric blur does not affect the effective spatial resolution.

3.4. Bragg edge profiles of corroded steel using energy-resolved imaging

To illustrate the improvement of the time-of-flight imaging setup for high resolution, a CO_2 corroded X65 steel sample was examined. The corroded sample has a siderite film with a thickness of close to 40 μm. Fig. 10a and b show the CO_2 corroded steel sample and the corresponding radiography using time of flight imaging technique at IMAT. Fig. 10c shows a simulation created in NxsPlotter [53] of attenuation as a function of wavelength considering neutrons passing through corrosion layers on the top surface of the steel sample. The simulations indicate significant Bragg edges (sharp transitions, Fig. 10c) for Fe (110) at 4 Å, and $FeCO_3$ (104) at 5.6 Å, which agree with the Bragg edge transmission profile plots for steel and siderite using both the MCP and LumaCam setups (Fig. 10d and e). The change in transmission values observed in Figs. 10d and e is due to a change in the ROI chosen, as well as change in the pixel size and field of view in both the setups. Comparison of Bragg edge spectra demonstrate visibility of steel and siderite Bragg edges for larger (>1 pixel) and smaller (1 pixel in one direction) ROI box widths (Fig. 10d and e). This indicates that siderite edges are clearly visible for 1-pixel resolutions across the corrosion film with both Bragg edge detectors, even though the MCP resolution is coarser than the width of the corrosion film. In comparison, the LumaCam allows

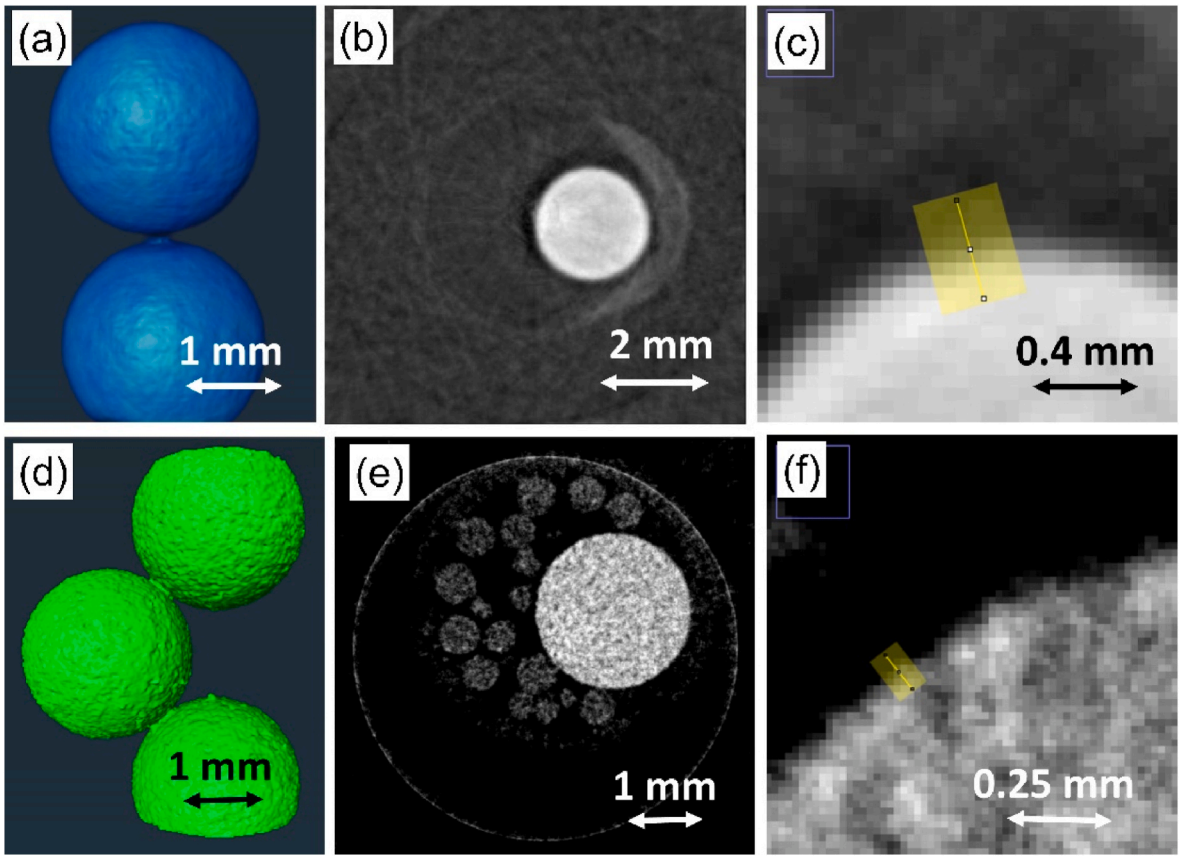

Fig. 8. (a) 3D volume of steel spheres (CCD setup); (b) corresponding reconstructed slice; 2 mm steel spheres (CCD setup); (c) selected edge for MTF analysis (CCD setup); (d) 3D volume of steel spheres (CCD + taper setup); (e) corresponding reconstructed slice; 2 mm steel spheres and 0.5 mm zirconia spheres are visible (CCD + taper setup); (f) selected edge for MTF analysis (CCD + taper setup).

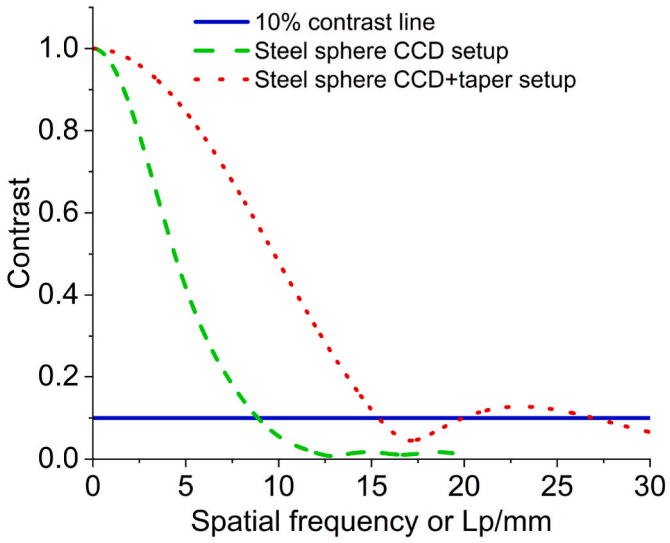

Fig. 9. Steel sphere MTF curves for CCD and CCD + taper setups.

imaging the siderite corrosion film with a finer resolution of 30 μm and an effective pixel size of 15 μm. Therefore, enhancement in resolution with the LumaCam setup allows for the detection of films thinner than 40 μm, improving its ability to resolve finer details. It can be noted that white beam data collection with the taper setup could not reveal the siderite film, due to low attenuation contrast, presence of geometric blur and due to edge effects. In comparison, the diffraction contrast provided by the Bragg edge detectors allowed detection of the corrosion film.

Table 4
Tabulated values of line pairs per mm and spatial resolution (from Fig. 9).

Setup	Sample details	Line pairs per mm (mm^{-1})	Resolution (μm)
CCD	Steel sphere Ø2 mm	8.88	56.3
CCD + taper	Steel sphere Ø2 mm	15.38	32.5

4. Conclusions

Limited spatial resolution is a key challenge encountered in neutron imaging for resolving thin films or coated materials (e.g., surface corrosion layers), even more so for in-situ studies on material degradation. Bragg edge imaging is advantageous for surface analysis, effectively differentiating between crystalline substrate and surface corrosion phases, and mitigating issues such as edge refraction effects. The results of this work demonstrate that the resolution on IMAT, which is flux-limited, can be improved by more than a factor of two using a fiber optics taper (FOT) for white-beam 3D imaging, while event centroiding was used to enhance the spatial resolution for 2D Bragg edge measurements by achieving sub-pixel resolution. Whilst a FOT reduces the field of view and detection efficiency, the second approach using Timepix holds a promise for improving spatial resolution with much higher efficiency for both white beam and energy-resolved imaging. Future improvements of spatial resolution on IMAT are anticipated through a fourfold increase of neutron flux with the installation of a planned

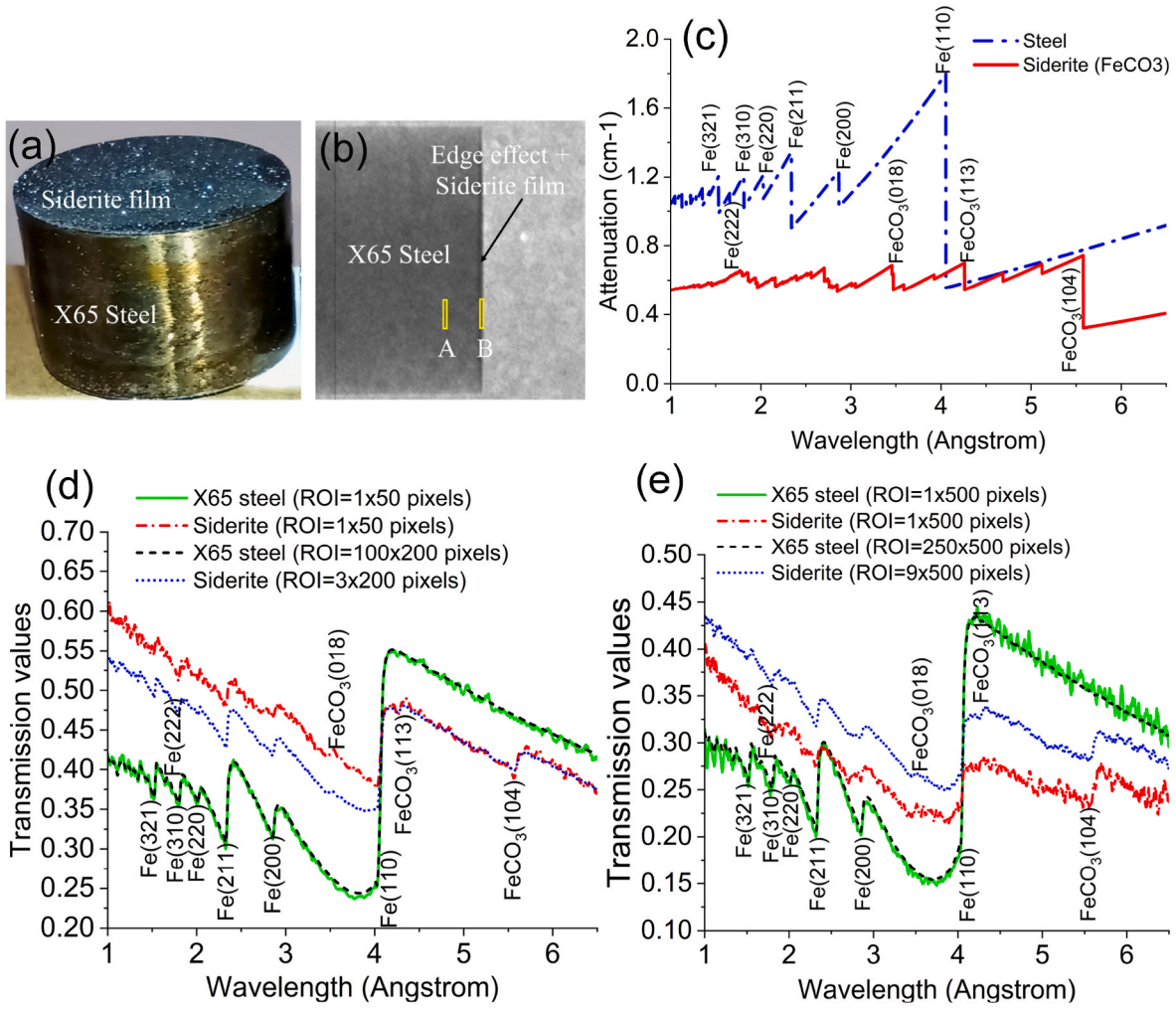

Fig. 10. (a) X65 steel sample with siderite corrosion film on the surface; (b) MCP radiogram of X65 steel sample for a wavelength of 4.2 Å. The vertical dark grey line at the position of the siderite film is partially due to the change in refraction of the material (edge effect); (c) Simulated attenuation curves of steel and siderite; (d) Transmission profiles of steel (region A from (b)) and siderite (region B from (b)) with selected ROI in pixels from MCP setup; (e) Transmission profiles of steel and siderite with selected ROI in pixels from LumaCam setup.

upstream sample position, alongside enhancements in detection efficiencies and vibration-free camera support of the detector systems.

CRediT authorship contribution statement

Vicky Ullas Mirashi: Writing – review & editing, Writing – original draft, Methodology, Data curation, Conceptualization. **Winfried Kockelmann:** Writing – review & editing, Supervision, Project administration, Methodology, Data curation, Conceptualization. **Nikil Kapur:** Writing – review & editing, Methodology, Data curation, Conceptualization. **Anna Fedrigo:** Writing – review & editing. **Manuel Morgano:** Writing – review & editing. **Thawatchart Chulapakorn:** Writing – review & editing. **Adrian Losko:** Writing – review & editing. **Alexander Wolfertz:** Writing – review & editing. **Anton S. Tremsin:** Writing – review & editing. **Adriana Matamoros-Veloza:** Writing – review & editing, Supervision, Project administration, Methodology, Investigation, Funding acquisition, Data curation, Conceptualization.

Funding

ISIS Neutron and Muon Source (501100021200) - ISIS Facility Development Studentship Programme; ISIS Neutron and Muon Source (501100021200) - DOI 10.5286/ISIS.E.RB2220699; Bundesministerium für Bildung und Forschung (501100002347) - 05K19WO2, 05K22WO5.

Declaration of competing interest

The authors declare that they have no known competing financial interests or personal relationships that could have appeared to influence the work reported in this paper.

Acknowledgements

Special thanks to Science and Technology Facilities Council (STFC) for providing funding and support to VUM to carry out the project work on IMAT (Imaging and Materials Science & Engineering) under the ISIS Facility Development Studentship Programme. The ISIS Neutron and Muon Source is acknowledged for access to neutron beam facilities (DOI 10.5286/ISIS.E.RB2220699). Many thanks to Dilshad Shaikhah, from the Institute of Functional Surfaces at Leeds, for providing a corroded steel sample for imaging. Two of us (A.L. and A.W.) gratefully acknowledge financial support from the BMBF in the framework of the research projects 05K19WO2 and 05K22WO5.

Appendix A. Supplementary data

Supplementary data to this article can be found online at https://doi.org/10.1016/j.nima.2025.170284.

Data availability

Data underlying the results presented in this paper are not publicly available at this time but may be obtained from the authors upon reasonable request.

References

[1] W. Reimers, A.R. Pyzalla, A. Schreyer, et al., Neutrons and Synchrotron Radiation in Engineering Materials Science, WILEY-VCH Verlag GmbH & Co. KGaA, Weinheim, 2008.

[2] P.J. Withers, Mapping residual and internal stress in materials by neutron diffraction, C. R. Phys. 8 (7–8) (Sep. 2007) 806–820, https://doi.org/10.1016/j.crhy.2007.09.015.

[3] S. Roshankhah, J.P. Marshall, A. tengattin, et al., Neutron imaging: a new possibility for laboratory observation of hydraulic fractures in shale? Géotech. Lett. 8 (4) (Dec. 2018) 316–323, https://doi.org/10.1680/jgele.18.00129.

[4] N. Kardjilov, I. Manke, A. Hilger, et al., Neutron imaging in materials science, Mater. Today 14 (6) (2011) 248–256, https://doi.org/10.1016/S1369-7021(11)70139-0.

[5] W. Treimer, Neutron tomography, in: Neutron Imaging and Applications, Springer US, Boston, MA, 2009, pp. 81–108, https://doi.org/10.1007/978-0-387-78693-3_6.

[6] K.W. Tobin, P.R. Bingham, J. Gregor, Mathematics of neutron imaging, in: Neutron Scattering Applications and Techniques ((*NEUSCATT)*, Springer US, Boston, MA, 2009, pp. 109–127, https://doi.org/10.1007/978-0-387-78693-3_7.

[7] IMAGING OPTICS - A technical source for imaging solutions'. [Online]. Available: www.edmundoptics.com/imaging..

[8] P. Boillat, G. Frei, E.H. Lehmann, et al., Neutron imaging resolution improvements optimized for fuel cell applications, Electrochem. Solid State Lett. 13 (3) (2010), https://doi.org/10.1149/1.3279636.

[9] M. Morgano, P. Trtik, M. Meyer, et al., Unlocking high spatial resolution in neutron imaging through an add-on fibre optics taper, Opt. Express 26 (2) (2018) 1809, https://doi.org/10.1364/oe.26.001809.

[10] P. Trtik, J. Hovind, C. Grünzweig, et al., Improving the spatial resolution of neutron imaging at Paul scherrer Institut - the neutron microscope project, in: Physics Procedia, vol. 69, Elsevier B.V., 2015, pp. 169–176, https://doi.org/10.1016/j.phpro.2015.07.024.

[11] A. Tengattini, N. Lenoir, E. Andò, et al., NeXT-grenoble, the neutron and X-ray tomograph in Grenoble, Nucl. Instrum. Methods Phys. Res. 968 (Jul) (2020), https://doi.org/10.1016/j.nima.2020.163939.

[12] A. Tengattini, N. Kardjilov, L. Helfen, et al., Compact and versatile neutron imaging detector with sub-4μm spatial resolution based on a single-crystal thin-film scintillator, Opt. Express 30 (9) (Apr. 2022) 14461, https://doi.org/10.1364/oe.448932.

[13] M. Arif, D.S. Hussey, E.M. Baltic, et al., Neutron imaging facility development and research trend at NIST, in: Physics Procedia, vol. 69, Elsevier B.V., 2015, pp. 210–217, https://doi.org/10.1016/j.phpro.2015.07.030.

[14] D.S. Hussey, J.M. LaManna, E. Baltic, et al., Neutron imaging detector with 2 μm spatial resolution based on event reconstruction of neutron capture in gadolinium oxysulfide scintillators, Nucl. Instrum. Methods Phys. Res. 866 (May 2017) 9–12, https://doi.org/10.1016/j.nima.2017.05.035.

[15] K. Isegawa, D. Setoyama, H. Kimura, et al., The first application of a Gd3Al2Ga3O12:Ce single-crystal scintillator to neutron radiography, J Imaging 7 (11) (May 2021), https://doi.org/10.3390/jimaging7110232.

[16] A. Faenov, M. Matsubayashi, T. Pikuz, et al., Using LiF crystals for high-performance neutron imaging with micron-scale resolution, High Power Laser Science and Engineering 3 (2015), https://doi.org/10.1017/hpl.2015.28.

[17] M.E. Moore, P. Trtik, J. Lousteau, et al., Neutron imaging with Li-glass based multicore SCIntillating FIber (SCIFI), J. Lightwave Technol. 37 (2019), https://doi.org/10.1109/JLT.2019.2934497.

[18] A.S. Tremsin, J.B. McPhate, J.V. Vallerga, et al., High-resolution neutron radiography with microchannel plates: proof-of-principle experiments at PSI, Nucl. Instrum. Methods Phys. Res. 605 (1–2) (Jun. 2009) 103–106, https://doi.org/10.1016/j.nima.2009.01.137.

[19] S. Tremsin, J.B. McPhate, J.V. Vallerga, et al., Detection efficiency, spatial and timing resolution of thermal and cold neutron counting MCP detectors, Nucl. Instrum. Methods Phys. Res. 604 (1–2) (May 2009) 140–143, https://doi.org/10.1016/j.nima.2009.01.041.

[20] T. Minniti, A.S. Tremsin, G. Vitucci, et al., Towards high-resolution neutron imaging on IMAT, in: Journal of Instrumentation, vol. 13, Institute of Physics Publishing, Jan. 2018, https://doi.org/10.1088/1748-0221/13/01/C01039.

[21] E. Calzada, F. Gruenauer, M. Mühlbauer, et al., New design for the ANTARES-II facility for neutron imaging at FRM II, Nucl. Instrum. Methods Phys. Res. 605 (1–2) (May 2009) 50–53, https://doi.org/10.1016/j.nima.2009.01.192.

[22] N. Kardjilov, A. Hilger, I. Manke, et al., Neutron tomography instrument CONRAD at HZB, Nucl. Instrum. Methods Phys. Res., Sect. A 651 (Sep. 2011) 47–52, https://doi.org/10.1016/j.nima.2011.01.067.

[23] D.S. Hussey, D.L. Jacobson, M. Arif, et al., New neutron imaging facility at the NIST, Nucl. Instrum. Methods Phys. Res. 542 (May 2005) 9–15, https://doi.org/10.1016/j.nima.2005.01.004.

[24] A.S. Tremsin, J.V. Vallerga, J.B. McPhate, et al., High resolution photon counting with MCP-timepix quad parallel readout operating at > 1 KHz frame rates, IEEE Trans. Nucl. Sci. 60 (2) (2013) 578–585, https://doi.org/10.1109/TNS.2012.2223714.

[25] R.S. Ramadhan, W. Kockelmann, T. Minniti, et al., Characterization and application of Bragg-edge transmission imaging for strain measurement and crystallographic analysis on the IMAT beamline, J. Appl. Crystallogr. 52 (2) (Apr. 2019) 351–368, https://doi.org/10.1107/S1600576719001730.

[26] A.S. Losko, Y. Han, B. Schillinger, et al., New perspectives for neutron imaging through advanced event-mode data acquisition, Sci. Rep. 11 (1) (Dec. 2021), https://doi.org/10.1038/s41598-021-00822-5.

[27] A. Fioravante, R.S. Nunes, H.A. Acciari, et al., Films formed on carbon steel in sweet environments - a review, Sociedade Brasileira de Quimica, https://doi.org/10.21577/0103-5053.20190055, 2019.

[28] Matamoros-Veloza, T.M. Stawski, S. Vargas, et al., Study of a local structure at the interface between corrosion films and carbon steel surface in undersaturated CO2 environments, ACS Omega 8 (9) (Mar. 2023) 8497–8504, https://doi.org/10.1021/acsomega.2c07631.

[29] T. Minniti, K. Watanabe, G. Burca, et al., Characterization of the new neutron imaging and materials science facility IMAT, Nucl. Instrum. Methods Phys. Res. 888 (Apr. 2018) 184–195, https://doi.org/10.1016/j.nima.2018.01.037.

[30] G.D. Boreman, Modulation Transfer Function in Optical and Electro-Optical Systems, TT52, A Publication of SPIE - The International Society for Optical Engineering, Bellingham, Washington USA, 2001.

[31] R. Woracek, J. Santisteban, A. Fedrigo, et al., Diffraction in neutron imaging—a review, Nucl. Instrum. Methods Phys. Res. 878 (Jan. 2018) 141–158, https://doi.org/10.1016/j.nima.2017.07.040.

[32] Oxford Instruments – ANDOR". Accessed: (Aug. 2024). [Online]. Available: https://andor.oxinst.com/..

[33] V. Finocchiaro, F. Aliotta, D. Tresoldi, et al., The autofocusing system of the IMAT neutron camera, Rev. Sci. Instrum. 84 (9) (Sep. 2013), https://doi.org/10.1063/1.4819793.

[34] E.R. Fossum, CMOS image sensors: electronic camera-on-A-chip. Proceedings of International Electron Devices Meeting, 1995, pp. 17–25, https://doi.org/10.1109/IEDM.1995.497174.

[35] H. Kobayashi, Design and basic character of neutron collimator on radiography, in: JAERI-conf, 99-006, 1999, pp. 367–372.

[36] Scintillators - Imaging using a neutron beam by RC Tritec". Accessed: (Aug. 2024). [Online]. Available: https://www.rctritec.com/en/isotopes/applications-1..

[37] Fiber Optics Taper by INCOM". Accessed: (Aug. 2024). [Online]. Available: https://incomusa.com/..

[38] P. Trtik and E. H. Lehmann, "Isotopically-enriched gadolinium-157 oxysulfide scintillator screens for the high-resolution neutron imaging", Nucl. Instrum. Methods Phys. Res. A, vol. 788, pp. 67–70, (Jul. 2015), https://doi.org/10.1016/j.nima.2015.03.076..

[39] W.B. Feller, R.G. Downing, P.L. White, Neutron field imaging with microchannel plates, in: Proceedings - Society of Photo-Optical Instrumentation Engineers, vol. 4141, 2000, pp. 291–302, https://doi.org/10.1117/12.407591.

[40] A.S. Tremsin, W.B. Feller, R.G. Downing, Efficiency optimization of microchannel plate (MCP) neutron imaging detectors. I. Square channels with 10B doping, Nucl. Instrum. Methods Phys. Res. 539 (1–2) (Feb. 2005) 278–311, https://doi.org/10.1016/j.nima.2004.09.028.

[41] A.P. Kaestner, Z. Kis, M.J. Radebe, et al., Samples to determine the resolution of neutron radiography and tomography, in: Physics Procedia, vol. 88, Elsevier B.V., 2017, pp. 258–265, https://doi.org/10.1016/j.phpro.2017.06.036.

[42] API 5L X Grades: X52 X56 X60 X65 X70 Welded & Seamless Pipe API 5LX", PM International Suppliers. [Online]. Available: https://www.api5lx.com/api5lx-grades/..

[43] S. Tygier, D. Akello-Egwel, J. Allen, et al., Tomographic reconstruction with Mantid imaging, in: Journal of Physics: Conference Series, Institute of Physics, 2023, https://doi.org/10.1088/1742-6596/2605/1/012017.

[44] Thermo Fisher ScientificTM, Avizo 3D 2023.1.1 [Online], http://www.thermofisher.com/amira-avizo. (Accessed 13 August 2024).

[45] D.A. Abbass, R.A. Abaas, A.M. Qnewie, et al., Study measurements MTF, LSF and ESF for the imaging system quality analysis, Int. J. Innov. Res. Sci. Eng. Technol. 8 (11) (2019). https://www.ijirset.com/upload/2019/november/7_Study.PDF.

[46] S.H. Williams, A. Hilger, N. Kardjilov, et al., Detection system for microimaging with neutrons, J. Instrum. 7 (2) (May 2012), https://doi.org/10.1088/1748-0221/7/02/P02014.

[47] J. Schindelin, I. Arganda-Carreras, E. Frise, et al., Fiji: an open-source platform for biological-image analysis, Nat. Methods 9 (7) (May 2012) 676–682, https://doi.org/10.1038/nmeth.2019.

[48] A. Schneider, W.S. Rasband, K.W. Eliceiri, NIH Image to ImageJ: 25 years of image analysis, Nat. Methods 9 (7) (May 2012) 671–675, https://doi.org/10.1038/nmeth.2089.

[49] M. Turkmenoglu, O. Sengul, L.B. Yalciner, MTF measurements for the imaging system quality analysis, gazi Univ. Sci. 25 (2012) 19–28 [Online], https://api.semanticscholar.org/CorpusID:109865846.

[50] K. Kohm, Modulation transfer function measurement method and results for the orbview-3 high resolution imaging satellite, Int. Arch. Photogram. Rem. Sens. Spatial Inf. Sci. 35 (Jan. 2004). https://api.semanticscholar.org/CorpusID:6472917.

[51] A.S. Tremsin, J.V. Vallerga, J.B. McPhate, et al., Optimization of Timepix count rate capabilities for the applications with a periodic input signal, in: Journal of

Instrumentation, vol. 9, Institute of Physics Publishing, JINST, May 2014, https://doi.org/10.1088/1748-0221/9/05/C05026.
[52] "OriginPro", Version 2024b. OriginLab Corporation, Northampton, MA, USA.' [Online]. Available: https://www.originlab.com/..
[53] M. Boin, Nxs: a program library for neutron cross section calculations, J. Appl. Crystallogr. 45 (3) (Jun. 2012) 603–607, https://doi.org/10.1107/S0021889812016056.